Encapsulation of bimetallic metal nanoparticles into robust Zr-based metal-organic frameworks: Evaluation of the catalytic potential for size-selective hydrogenation

Christoph Rösler,[a] Stefano Dissegna,[b] Victor L. Rechac,[c] Max Kauer,[a] Penghu Guo,[f] Stuart Turner,[e] Kevin Ollegott,[f] Hirokazu Kobayashi,[g] Tomokazu Yamamoto,[h] Daniel Peeters,[a] Yuemin Wang,[d] Syo Matsumura,[h] Gustaaf Van Tendeloo,[e] Hiroshi Kitagawa,[g] Martin Muhler,[f] Francesc X. Llabrés i Xamena*[c] and Roland A. Fischer*[b]

Abstract: The realization of metal NPs with bimetallic character and distinct composition for specific catalytic applications is an intensively studied field. Due to the synergy between metals, most of the bimetallic particles exhibit unique properties, only hardly provided by the individual monometallic counterparts. However, as small sized NPs possess high surface energy, agglomeration during catalytic reactions is favored. Sufficient stabilization can be achieved by confinement of NPs in porous support materials. In this sense, especially MOFs gained a lot of attention during the last years, however, encapsulation of bimetallic species remains challenging. Herein, the exclusive embedding of preformed core/shell PdPt and RuPt NPs into chemically robust Zr-based MOFs is presented. Microstructural characterization manifests partial retention of the core/shell systems after successful encapsulation without harming the crystallinity of the microporous support. The resulting chemically robust NP@UiO-66 materials exhibit enhanced catalytic activity towards the liquid-phase hydrogenation of nitrobenzene, competitive with commercially used Pt on activated carbon, but with simultaneous superior size-selectivity for sterically varying substrates.

Introduction

The utilization of metallic nanoparticles (NP) and reactive species within porous materials is of great interest, due to a broad field of applications.[1-3] Especially the synthesis and encapsulation of bimetallic moieties with controlled size, morphology and composition inside highly stable metal-organic frameworks (MOFs) exhibit potential for improved activity and selectivity in heterogeneous catalysis.[4-6] MOFs are a relatively new class of crystalline, porous materials with individual and tunable properties in each structure.[7] Consisting of functional organic entities connected to metal clusters, multi-dimensional structures with large inner pore volume and a defined micro- or mesoporosity can be obtained.[8-9] Hence, MOFs are appropriate candidates for the stabilization of active NPs together with molecule/substrate selective properties, due to the individual and regular framework pore structure.

On the other hand, the well-established bottom-up synthesis of NPs allows a variety of combinations of different metals.[10] The most prominent examples for bimetallic NPs are alloys, also known as solid solutions, with a random distribution of two or more metals within the NP, and core/shell particles with a defined interface of the core and shell metal.[11-13] In case of core/shell systems it is known that the inner metal core significantly influences the external shell of the second metal and therefore provides unique synergetic effects and physicochemical properties.[14] However, so far the exclusive encapsulation of bimetallic NPs with controlled composition into MOFs is challenging and only a few examples are known.[4-5, 15-19] The synthesis of such systems includes for example the use of chemical vapor infiltration[4], decomposition of linker-bonded metal complexes[17-18] or the encapsulation of preformed NPs by a template synthesis.[15, 19] Particularly, the template approach offers some

advantages compared to the other strategies. This involves i) controlled encapsulation of particles within the framework with avoidance of undesired particle formation at the outer surface of the host, suitable for size-selective catalytic reactions, and ii) control of the exact NP size, morphology and composition by well-established synthetic routes.[20-21] However, one important factor is the compatibility of the solvothermal MOF synthesis and the stability of the NPs at the same time. Recently, Zhang et al. have established a synthesis for the encapsulation of Pt NPs into the highly stable UiO-66.[22] This framework belongs to the group of Zr-based MOFs, offering a three-dimensional pore system with two types of cavities.[23-24] Moreover, it features high adjustability of the pore volume and linker functionality.[25-26] However, to best of our knowledge, no examples for the encapsulation of bimetallic NPs with controlled composition into UiO-66-type materials are known so far. One reason for this is the relatively small pore aperture (~ 6 Å), which excludes a number of possible organometallic precursors, as well as the high reactivity of the Lewis-acidic sites and the hydroxy groups, which are bonded to Zr-cluster inside the framework. Previously, it was shown that the incorporation of Pd NPs via chemical vapor infiltration is strongly depending on the infiltration temperature.[24] Only at low temperatures (-10 °C), sufficient encapsulation of NPs inside UiO-66 and UiO-67 was possible. However, the applied conditions allow the infiltration of the metal precursor only within a long time frame, due to temperature depending deceleration, and the spatial distribution of the particles was partially inhomogeneous.

Certainly, in case of template synthesis, the solvothermal conditions of the MOF dictate the type of useable preformed NPs. For instance, during the synthesis of Zr-based MOFs hydrochloric acid is produced from commonly used precursors (e.g. $ZrCl_4$), which in fact dissolves a large number of metal NPs and therefore prevents an effective encapsulation. One strategy to overcome this problem is the use of alternative Zr-based precursor (e.g. zirconium propoxide), e.g. for the encapsulation of hydrochloric acid sensitive Au NPs as shown by Tulig et al.[27] However, the resulting materials suffer from strong particle growth and incomplete encapsulation with large numbers of particles at the outer surface, ineffective for size-selective catalysis.

The present absence of examples with bimetallic NPs in Zr-based MOFs was the motivation for us to exclusively encapsulate bimetallic nanoparticles into UiO-66 by a protective strategy, without resignation of the important precursor $ZrCl_4$. As mentioned above, Pt NPs can be encapsulated into the target host UiO-66 as their stability is high enough to resist hydrochloric acid. This fact prompted us to implement a protective, stabilizing Pt shell around more labile particles, which enables the incorporation of bimetallic species even under the harsh solvothermal conditions of the UiO-66 synthesis (Scheme 1).

Initially, the encapsulation of catalytically active Pd NPs was aimed, because they own promising properties for several catalytic processes.[28] However, no suitable systems with exclusively embedded Pd NPs, due to dissolution of small sized Pd NPs (~ 3 nm) during solvothermal MOF growth, could be obtained. Hence, the introduction of bimetallic NPs with Pt as the second metal was aspired. It is known that modification of the core material by a shell can influence core specific properties, such as reactivity and thermal stability and, consequently, enhances the overall particle stability.[13]

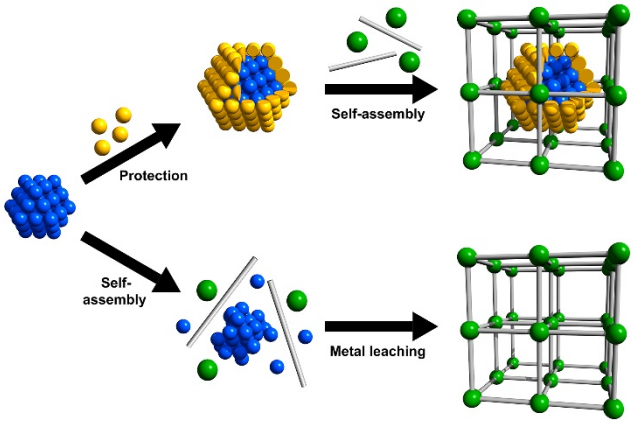

Scheme 1: Illustration of the template based embedding of metal NPs into MOFs starting from monometallic NPs. Encapsulation of particles succeeded only in case of stabilization by a protective layer of a second metal, while the monometallic particles were leached during the solvothermal synthesis of the MOF and result in particle free crystals mainly. Color coding: green, secondary building units of the MOF; grey, organic linkers; blue and yellow, metal atoms of the NPs.

Herein, the effective core-located encapsulation of surfactant-stabilized bimetallic PdPt NPs into the Zr-based MOF, UiO-66, by template synthesis was investigated for the first time. The resulting materials exhibit substrate specific size-selectivity and simultaneously improved catalytic activity for the hydrogenation of different nitrobenzene derivatives, compared to embedded monometallic counterparts, as also shown by Zhang et al.[29] Furthermore, the transferability of the concept to other terephthalate based systems with amino- or nitro-functionality was investigated and other bimetallic core/shell particles (RuPt) were successfully incorporated into UiO-66 as well.

Results and Discussion

Initially, the encapsulation of Pd NPs with a size of 3-5 nm was considered. The particles were produced by reduction of H_2PdCl_4 in aqueous ethanolic solution in presence of polyvinylpyrrolidone (PVP). For the synthesis of the metal-loaded UiO-66 structures, a solvothermal approach with the addition of metal NPs was applied. Generally, $ZrCl_4$ and acetic acid were mixed in DMF and sonicated until full dissolution. Afterwards, terephthalic acid was added and dissolved. Finally, the Pd NPs were dispersed in DMF, added with subsequent agitation and the mixture was kept in an oven at 120 °C for 24 h. During the synthesis the original brown color (Pd NPs) of the mixture disappears, resulting in a colorless, clear solution. This fact indicates leaching of the used Pd NPs. The resulting white precipitate was investigated by transmission electron microscopy (TEM) to elucidate if low quantities of Pd NPs are still present (Figure S1). The images indicate the formation of well-shaped MOF nanocrystals, however, without the visible presence of Pd NPs inside the crystallite cores. Only few agglomerated Pd nanocrystals with broad size distribution were detected on the outer surface of MOF crystallites, which supports the observed phenomenon of leaching. Therefore, the encapsulation process was replaced by PdPt core/shell NPs with Pt as the second metal for enhanced stability towards agglomeration and leaching. PVP functionalized bimetallic nanoparticles as well as monometallic Pt NPs were produced by established synthetic strategies. The Pt NPs were synthesized by alcohol based reduction of the corresponding metal salt H_2PtCl_6, yielding particles with a size

of approximately 3 nm. Bimetallic core/shell PdPt NPs were fabricated by a hydrogen-sacrificial protective approach, as described by Wang et al.[30] A colloidal NP solution of the core metal Pd was successively coated with Pt atoms under ambient temperature in hydrogen atmosphere. The introduced H2 dissociates on the Pd NP surface, while in a second step an aqueous Pt salt solution is slowly added, where Pt ions reduce predominately at the surface of Pd NPs due to dissociated surface hydrogen atoms and form a shell on top. Following this synthetic approach bimetallic PdPt NPs with different metal ratios (Pd:Pt, 1:1 and 1:2) were produced. After purification and drying, the particles were encapsulated into UiO-66 similar to the previously described method for the incorporation of Pd NPs. The resulting samples were denoted as Pd1Pt1@UiO-66 and Pd1Pt2@UiO-66, while also Pt@UiO-66 with a monometallic species was produced. All samples retain their dark-brown color during the solvothermal synthesis. After 24 h, grey (Pt@UiO-66) and brownish-blackish (PdPt@UiO-66) precipitates with clear, colorless supernatant were obtained.

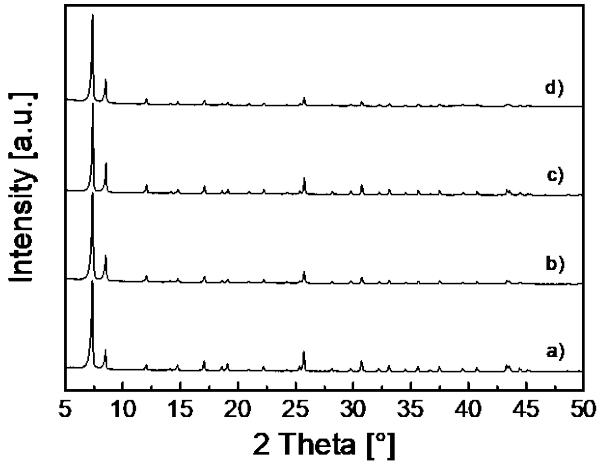

Figure 1. Powder XRD patterns of b) Pt@UiO-66, c) Pd1Pt1@UiO-66 and d) Pd1Pt2@UiO-66, in comparison to pristine UiO-66 (a).

After washing and solvent exchange with MeOH the samples were dried in vacuum at room temperature. Initial characterization was done by powder x-ray diffraction (XRD). The corresponding patterns of the NP@UiO-66 composites indicate the expected position of the two intense (111) and (200) reflections of UiO-66 at 2 = 7.4 and 8.5°, analogous to pristine UiO-66 and therefore verify the intact structure after the encapsulation process (Figure 1).[23] In case of the metal NP containing materials no additional signals for the corresponding metal NPs in the range of 2 = 38 – 46° were observed. This might be due to the small size of the particles as well as the low loading quantity. For clarity TEM measurements were performed.

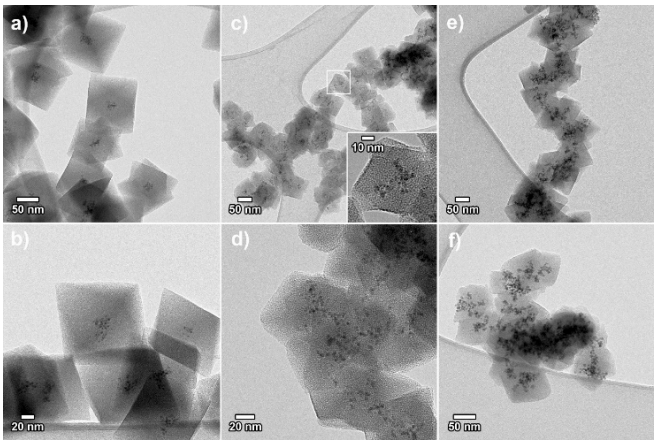

Figure 2. Bright field TEM images of the metal loaded composites Pt@UiO-66 (a, b), Pd1Pt1@UiO-66 (c, d) and Pd1Pt2@UiO-66 (e, f). c) Magnification of the area labeled by the white frame shows the presence of core-located, small sized bimetallic PdPt NPs.

The images indicate successful encapsulation of NPs into the core of the formed UiO-66 crystals for all samples. Compared to Pt@UiO-66 (Figure 2a – b), the samples with the bimetallic species (Figure 2c – f) show higher tendency for coadunate and intergrown crystals. In case of Pt@UiO-66 and Pd1Pt1@UiO-66 the particles are exclusively encapsulated inside the MOF crystallites, while Pd1Pt2@UiO-66 indicates partial deposition at the outer surface. However, this phenomenon was observed rarely among all the investigated images of different section of the samples and effects on the size-selective catalysis should be negligible.

The preformed core Pd NPs exhibit a size of 3.4 ± 0.6 nm (Figure S2, left). Upon addition of a Pt shell, increase of the particle size with rising Pt content was expected. The evaluation of the NP sizes by TEM confirms this assumption with average NPs sizes of 4.2 ± 0.8 nm for Pd1Pt1@UiO-66 and 4.8 ± 0.7 nm for the composite with a thicker Pt shell (Pd1Pt2@UiO-66). For monometallic Pt particles inside UiO-66 an average size of 3.1 ± 0.4 nm was estimated, which is in accordance to literature (Figure S2, right).[22] Atomic absorption spectroscopy reveals the expected atomic ratio of Pd and Pt. The obtained results were also supported by electron-dispersive X-ray (EDX) spectroscopy measurements as summarized in Table 1.

Table 1. Metal ratio between Pd and Pt inside the samples Pd1Pt1@UiO-66 and Pd1Pt2@UiO-66, determined by elemental analysis and energy-dispersive x-ray spectroscopy (brackets).

	Pd	Pt
Pd_1Pt_1@UiO-66	55 (54)	45 (46)
Pd_1Pt_2@UiO-66	36 (38)	64 (62)

Interestingly both type of particles with thin and thick shell could be incorporated without any visible leaching. Clarification of the NP structure (core/shell or other), with exact location of Pd and Pt metals, after the encapsulation process was given by annular dark field scanning transmission electron microscopy (ADF-STEM) coupled with energy dispersive x-ray (EDX) spectroscopy. The obtained elemental maps support the presence of core/shell NPs after the incorporation.

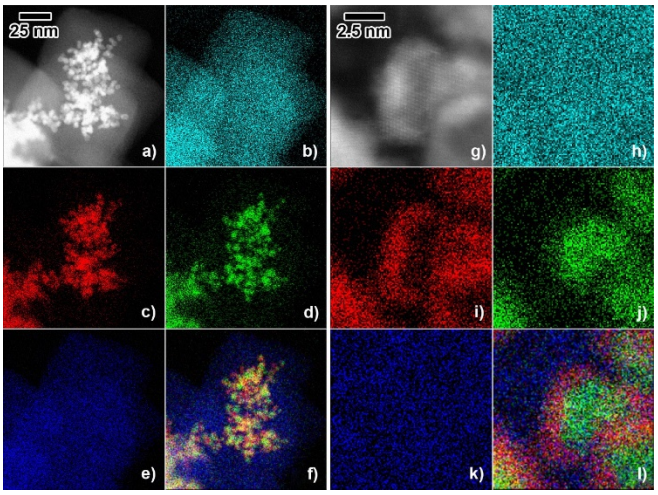

Figure 3. Left: a) ADF-STEM image of Pd1Pt1@UiO-66. b) - e) Two-dimensional elemental maps of O (cyan), Pt (red), Pd (green) and Zr (blue). f) Overlay image of the Pt, Pd and Zr maps. Right: g) High-resolution ADF-STEM image of in UiO-66 embedded Pd1Pt1 NPs. h) – k) Elemental maps of O (cyan), Pt (red), Pd (green) and Zr (blue). f) Overlay image of the Pt, Pd and Zr maps.

ADF-STEM measurements of the encapsulated Pd1Pt1 NPs into the Zr-based MOF illustrate the exact spatial arrangement of Pd and Pt inside the particles (Figure 3). The images (Figure 3i–l) show the presence of Pd (green) preferentially in the NP core while an enrichment of Pt (red) in the shell of the particles is displayed. The estimated size of the shell is roughly 1 nm, which is in accordance to the estimated average NP size (4.2 nm), compared to pre-synthesized Pd NPs (3.4 nm). However, the overview maps implicate also, that some Pd core particles are only partially covered with Pt, as the shell might be very thin and not clearly detectable by EDX mapping, due to the small size of particles (Figure 3c–f). Therefore, enrichment of Pd atoms in the Pt shell cannot be excluded. Besides, STEM-EDX maps illustrate the embedding of NPs into a Zr and O based (blue, cyan) matrix, namely UiO-66, which provides evidence for the successful encapsulation of the particles into the framework.

These observations were supported by low temperature CO adsorption measurements (UHV-FTIR), comparing the materials with thinner (Pd1Pt1@UiO-66) and thicker (Pd1Pt2@UiO-66) Pt shell (Figure S3). Exposing the clean Pd1Pt2@UiO-66 sample to CO at 100 K leads to the appearance of a major IR band at 2184 cm-1 and a minor IR band at 2153 cm-1, corresponding to CO adsorbed at parent Zr4+ and electronically modified Zr4+ sites, respectively. In addition, several bands corresponding to CO adsorbed at the PdPt core/shell particles can be found. The intense band at 2061 cm-1 is characteristic for linearly adsorbed CO at metallic Pt, while the weak and broad band with its maximum around 1850 cm-1 is characteristic for CO at isolated Pt in a bridged configuration. Additionally a very weak band at 1945 cm-1 can be assigned to CO adsorbed at a small amount of Pd that might be diffused through the Pt shell towards the nanoparticle surface or is not completely covered with Pt.[30] In contrast, the CO adsorption measurements of Pd1Pt1@UiO-66 with thinner shell reveal a more complex situation of the particle surface. Similar IR absorption bands corresponding to adsorbed CO at Zr4+ (2184 cm-1) and electronically modified Zr4+ sites (2153 cm-1) as well as a broad signal at 2068 cm-1 for linearly adsorbed molecules on Pt were observed. However, the bands for CO adsorbed at exposed Pd is in this sample more intense compared to Pd1Pt2@UiO-66, indicating a higher amount of Pd particles at the nanoparticle surface. The broad low-lying band (1980 to 1820 cm-

1) can be assigned to different CO modes on Pd and Pt. The shoulder at 1850 cm-1 corresponds to bridged CO on Pt, while the vibrational bands at 1960, 1925 and 1885 cm-1 are characteristic for bridged-bonded CO–Pd complexes. This supports our assumption that the sample with higher Pd:Pt ratio of 1:1 exhibits a thinner Pt shell, compared to the sample with a Pd:Pt ratio of 1:2, which has a Pt enriched surface. Consequently, thinner Pt shells result in a higher level of Pd diffusion towards the nanoparticle surface and therefore alloyed-like surfaces of Pt and Pd seem to be present. Similar observations were also reported by Rades et al. for bimetallic Pt-Pd supported zeolites, where the bimetallic NP surface was composed from both Pd and Pt atoms.[31]

X-ray photoelectron spectroscopy (XPS) was measured (Figure S4). The survey XPS spectrum of Pd1Pt1@UiO-66 reveals the presence of Zr, O and C, without additional signals for Pd and Pt. The absence of signals for Pd and Pt is most likely due to the surface sensitivity of XPS, thus confirm the full encapsulation of Pd/Pt NPs into the host matrix. XPS measurements after sputtering show the appearance of an additional signal for Pt 4f (Figure S4c), which was not detected before (Figure S4b). The two peaks at 71.3 and 74.6 eV correspond to Pt 4f7/2 and Pt 4f5/2, confirming the metallic character of Pt0.[32-33] Signals for Pd could not be specified because of the overlap of the Pd 3d peak (highest intensity) around 335 eV with the broad Zr 3p3/2 signal at 333 eV.[34]

Thermogravimetric analysis (TGA) of all samples was performed (Figure S5). The PdPt@UiO-66 samples, including the pristine UiO-66, show a decomposition temperature higher than 460 °C. Nevertheless, the thermal stability of the bimetallic samples is approximately 40 to 50 °C lower, as compared to the non-loaded MOF. Destabilization might be attributed to the not ideally grown MOF structure in the proximate vicinity of the PVP-protected NPs, as well as PVP chain movement and decomposition. This effect occurs more clearly in case of the Pt loaded hybrid material. Decomposition takes place at around 420 °C, while the prior mass loss (290 to 420 °C) can be explained by the decomposition of encapsulated PVP. This observation is in accordance to literature as the stability of NP bounded PVP is decreased.[35] It has to be mentioned that the Pt NPs were synthesized with higher metal:surfactant ratio to ensure sizes around 3 nm. Even though all particles were washed thoroughly to remove the excess of PVP, it is assumed that slightly higher PVP quantities were present at the Pt NP. FTIR measurements support this conjecture (Figure 4).

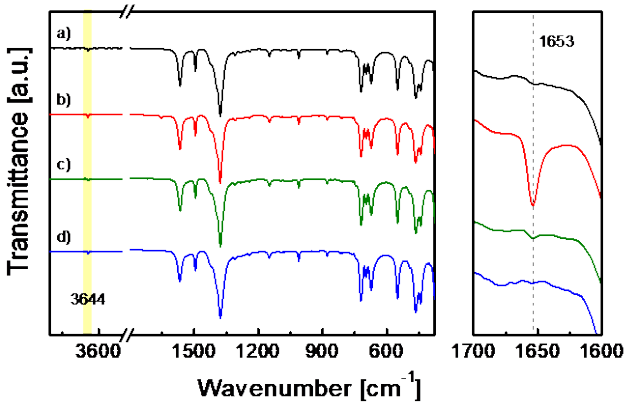

Figure 4. Left: FTIR spectra of a) pristine UiO-66 (black), b) Pt@UiO-66 (red), c) Pd1Pt1@UiO-66 (green) and d) Pd1Pt2@UiO-66 (blue). The yellow bar at 3644 cm-1 indicates the (O-H) stretching

of Zr-cluster bonded hydroxy groups. Right: Enlarged FTIR spectra of the respective samples in the range from 1700 to 1600 cm-1. The dashed line indicates the region of the (C=O) stretching vibration of PVP.

Pt@UiO-66 shows a weak band at 1653 cm-1, which can be assigned to the □(C=O) stretching vibration of incorporated PVP (Figure 4, right). Regarding the composites with bimetallic NPs, the signal is only weakly (Pd1Pt1@UiO-66, green) or not detected (Pd1Pt2@UiO-66, blue). Moreover, the FTIR measurements verify the integrity of all materials. The intense signals at 1567 and 1379 cm-1 correspond to the in- and out-of-phase stretching of the carboxylate groups in UiO-66.[23] Due to the drying procedure at room temperature the typical □(OH) vibration of the Zr bonded OH groups can be observed at 3644 cm-1 (yellow bar).

The permanent porosity of the samples was confirmed by nitrogen-sorption measurements (Figure S6). All isotherms show a type I behavior typical for microporous MOFs, such as UiO-66 with a pore window of 6 Å and cavity sizes of 8 Å and 11 Å for the tetrahedral and octahedral pore, respectively. Compared to the reference sample UiO-66, the metal-loaded samples exhibit slightly decreased Brunauer–Emmett–Teller (BET) surface areas (Table 2).

Table 2. BET surface area and noble metal loading quantity of the representative samples UiO-66, Pt@UiO-66, Pd1Pt1@UiO-66, and Pd1Pt2@UiO-66.

	UiO-66	**Pt@UiO-66**	**Pd_1Pt_1@UiO-66**	**Pd_1Pt_2@UiO-66**
Surface area [m^2/g]	1135	1108	1039	1024
Metal content [wt.%]	0	1.1	4.4	5.3

The difference of the measured surface area of all materials is rather small, compared to pristine UiO-66 (□max ~ 100 m2/g), even though the loading was with up to 5 wt.% of noble metals relatively high. This shows another advantage of the used template synthesis method, providing that the excess of stabilizing polymer was removed from the particle surface. With most of the post-encapsulation techniques (chemical vapor infiltration, solution impregnation), also including in-situ incorporation of linker bonded metals and subsequent decomposition, a significant decrease of a several hundreds of m2/g can be observed, even with small metal loadings from 0.5 to 2 wt.%. Considering that the loading amount of a non-porous metal inside a porous system is as low as 0.5 wt.%, no significant decrease of the surface area should occur. Therefore, the observed phenomenon can be attributed to occupation of pores, but more importantly to efficient pore blocking.[18] Additionally, the precursor decomposition procedure itself can harm the host. Hence, several sections of the MOF are not and/or only weakly accessible for guest molecules. In fact this observation is partially avoided, when the particles are overgrown by the porous framework, as the second step (precursor decomposition) is not required and, therefore, the chance for impairment of the framework structure is minimized.

In order to demonstrate the applicability of the concept to other materials, the encapsulation procedure of the core/shell PdPt NPs was also applied to two isoreticular Zr-based systems with amino and nitro functionalized linkers. Therefore, solvothermal synthesis similar to the non-functionalized UiO-66 was performed, but terephthalic acid was substituted by 2-

aminoterephthalic acid and 2-nitroterephthalic acid, respectively. The resulting materials PdPt@UiO-66-NH2 and PdPt@UiO-66-NO2 show high crystallinity after the encapsulation process, as verified by powder XRD measurements (Figure S7). The reflections of the amino and nitro derivative of UiO-66 match with those of the pure MOF and, likewise to the XRD patterns of PdPt@UiO-66, no additional signals corresponding to the embedded NPs were detected. Confirmation of the successful incorporation of NPs was provided by electron microscopy. The TEM images show well grown partially intergrown UiO-66-NH2 crystals with sharp edges and core-located NPs (Figure S8 a-b). In case of UiO-66-NO2, similar results were observed (Figure S8 d-e). Interestingly, the morphology of the synthesized crystals tends to be more spherical with no distinct crystal edges and a number of nanocrystals (~ 50 nm) without encapsulated NPs can be observed. Nevertheless, all PdPt NPs seem to be preferentially imbedded into the crystal core. The presence of Pd and Pt was confirmed by EDX measurements (Figure S8 c and f, UiO-66-NH2 and UiO-66-NO2 respectively). Signals for Pd were observed at 2.9 keV (L□), while Pt was detected at 9.4 (L□) and 11.1 keV (L□). Other detected elements were C, N, O, Zr, caused by the corresponding UiO-66 derivatives. Therefore, successfully extension to other Zr-terephthalate based MOFs was demonstrated.

The obtained results demonstrate the possibility for the incorporation of bimetallic PdPt NPs into UiO-66 under the harsh solvothermal conditions. Further studies on the encapsulation of RuPt core/shell NPs were done. Prior to the encapsulation process into UiO-66, preformed core/shell RuPt NPs were synthesized by a sequential deposition process of Ru and Pt in ethylene glycol (EG) according to Alayoglu et al.[36] First Ru(acac)3 (ruthenium acetylacetonate) was reduced at elevated temperatures in EG. In a subsequent step, PtCl2 was added and the reaction mixture was allowed to react for another 3 h with slowly increasing temperature up to reflux. Due to the slow heating ramp deposition of reduced Pt on the surface of the Ru seeds was favored. In this way, particles with metal ratios of Ru1Pt1 and Ru1Pt2 were synthesized. Incorporation of the particles was done with a similar method than for the PdPt NPs, resulting in the materials Ru1Pt1@UiO-66 and Ru1Pt2@UiO-66. Characterization by powder XRD indicates the intact structure of both metal@MOF composites without detection of embedded RuPt NPs, in terms of a broad signal around 2□ ≈ 40° (Figure S9). FTIR measurements support the integrity of the structures compared to pristine UiO-66 and no band for the presence of PVP at approximately 1650 cm-1 was detected (Figure S10). The permanent porosity of the samples was verified by N2-sorption measurements (Figure S11). Both NP@UiO composites exhibit type I isotherms and the determined BET surface areas were 997 m2g-1 for Ru1Pt1@UiO-66 and 1026 m2g-1 for Ru1Pt2@UiO-66 with a metal loading of 2.3 and 3.1 wt.%, respectively, according to atomic absorption spectroscopy. Exact calculation of the atomic ratios shows a deviation from the expected atomic ratios of Ru and Pt within the composite. The measured ratios of Ru and Pt of both samples were 38:62 (expected 50:50) and 26:74 (expected 34:66) with a decreased quantity of Ru.

Further evaluation of the materials was done by electron microscopy. The images verify the encapsulation of NPs into the core of the UiO-66 crystals (Figure S12). In both cases the generated crystals show spherical shapes without distinct edges. Especially the crystals of the composite with a higher Pt quantity exhibit frayed borders. EDX elemental maps of a loaded crystal (Ru1Pt1@UiO-66) confirm the presence of Zr, Ru and Pt, with a lower signal quantity for Ru (Figure S13). However, the exact particle composition (core/shell or different) could not be distinguished by elemental mapping. Therefore, high-resolution ADF-STEM images of the NPs were monitored. The images verify the formation of core/shell particles with distinct boundary between the Ru core and Pt shell (Figure S14a – b). Besides RuPt NPs, pure Pt NPs were partially

detected, probably originating from the alongside reduction of Pt precursor without deposition on the Ru cores (Figure S14c). The distance between adjacent lattice fringes was determined to be ~ 0.23 nm, which fits well with the distance between the (111) planes of fcc Pt. The estimated particle size after incorporation was found to be 4.2 ± 0.6 and 4.7 ± 0.6 nm for Ru1Pt1@UiO-66 and Ru1Pt2@UiO-66, respectively. These findings are in accordance to the size of the PdPt NP after encapsulation. Thickening of the Pt shell results in growth of the NPs and the size of the initial Ru seed NPs (3.3 nm) was found to be rather similar to those of Pd NPs (3.4 nm).

Evaluation of the size-selective hydrogenation potential of encapsulated PdPt NPs

The catalytic efficiency of the PdPt NP loaded composites compared to monometallic Pt was tested towards the hydrogenation of nitrobenzene based compounds. The resulting amino derivatives represent an important raw material and intermediate for many fine chemicals, pharmaceuticals, polymers or dyes.[37] These aromatic amines can be produced from the corresponding nitroarenes by catalytic hydrogenation, being various transition metals (viz., Pt,[38] Pd[39] and Ni,[40] either finely dispersed or adsorbed onto inert supports such as carbon or alumina) the most common catalysts used since long ago. Nowadays, however, most efforts are devoted to the design of new highly selective catalysts, including immobilized Au nanoparticles[41] and Au complexes,[42] which are able to reduce selectively the nitro group even in the presence of other reducible functional groups. Therefore, efficient and recyclable catalysts for the transformation of those nitro compounds to the corresponding amines are of great interest. The catalytic reactions were performed at room temperature under hydrogen atmosphere (p(H2)= 0.2 MPa) in hexane. In order to evaluate size/shape selective properties of the material, competitive hydrogenation experiments with two substrates, nitrobenzene (NB) and 3,5-dimethylnitrobenzene (dmNB), were utilized. The estimated smallest diameter of NB is approximately 5.8 Å, similar to that of benzene, while the one from dmNB is about 6.8 Å. Therefore, the microporous UiO-66 structure with a pore opening of 6 Å allows basically only the infiltration of the smaller molecule, which could then subsequently be hydrogenated by the embedded NPs. For comparison of the size-selective catalytic performance commercially available Pt NPs on carbon (Pt/C), monometallic Pt NPs in UiO-66 (Pt@UiO-66) and the parent UiO-66 were also tested. Unfortunately, testing of a comparable system with encapsulated Pd NPs was not possible due to the above mentioned agglomeration and leaching problems during the solvothermal synthesis of UiO-66. In case of UiO-66 without encapsulated NPs, no conversion of NB or dmNB was observed after 24 h. Figure 5 parts a and b show the catalytic results of the hydrogenation of the pure substrates to the respective anilines, while parts c and d correspond to the competitive hydrogenation of equimolar mixtures of both substrates.

The catalytic conversion of NB reveals that the material with bimetallic NPs (Pd1Pt1@UiO-66) exhibit enhanced activity for the conversion of NB to aniline with a performance comparable to Pt/C (Figure 5a). In contrast, the activity of the monometallic embedded Pt NPs was found to be lower. This fact proofs the synergetic effects between Pd and Pt atoms in the bimetallic species. Zhang et al. found similar trends for octahedral core/shell PdPt NPs during the hydrogenation of 4-chloronitrobenzene.[29] It should be noted that the material Pd1Pt1@UiO-66 fully reduces NB quantitatively to aniline within 2 h at room temperature with a metal:substrate ratio of 1:800, which is superior to the previously synthesized Pd@UiO-67 system. The Pd@UiO-67

composite was achieved via incorporation of a Pd-metalated linker (2,2'-bipyride-5,5'-dicarboxylic acid), where the Pd(II) complex was subsequently reduced at moderate temperatures to yield small sized Pd NPs inside the intact framework.[43] Therefore, effective etching of particles was avoided by post-synthetic formation of the NPs as it was also the case for other Pd-loaded Zr-MOFs.[24]

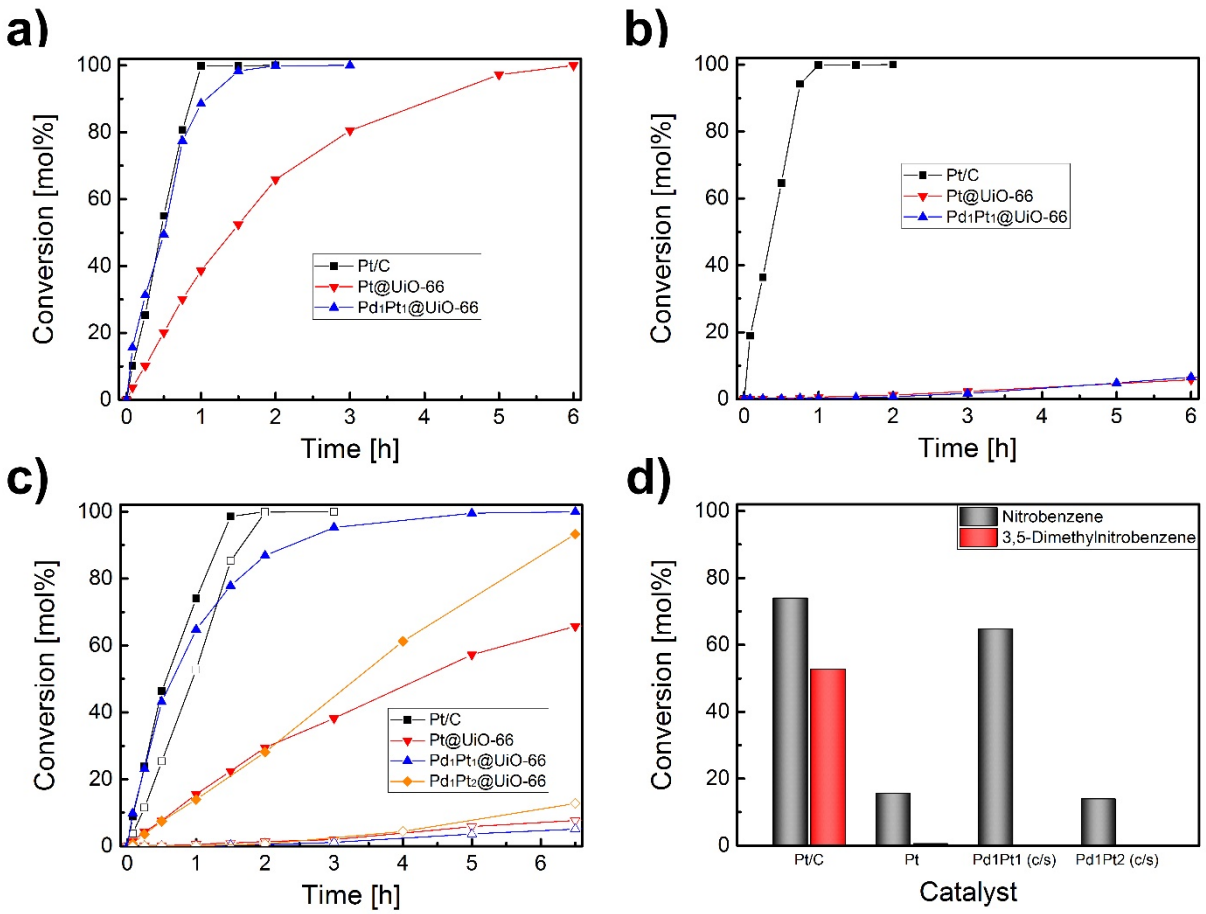

Figure 5. Time-conversion plot of a) nitrobenzene and b) 3,5-dimethylnitrobenzene in separated reactions. c) Simultaneous conversion of nitrobenzene (closed symbols) and 3,5-dimethylnitrobenzene (open symbols) in a one-pot reaction. d) Conversion of nitrobenzene (black bars) in comparison to 3,5-dimethylnitrobenzene (red bars) after 1 h over the catalysts Pt/C, Pt@UiO-66, Pd_1Pt_1@UiO-66 and Pd_1Pt_2@UiO-66. The graph represents the catalytic conversion of both substrates simultaneously. Reaction conditions: 25 °C, $p(H_2)$ = 0.2 MPa, hexane.

Investigation of the molecular size-selective catalytic properties was realized by use of the sterically more demanding molecule dmNB. Pt/C exhibits a similar conversion activity for dmNB compared to NB, while the NP@UiO-66 composites are almost inactive within the first 3 h (Figure 5b). Comparison of the catalysts after 1 h indicates a conversion of >99 % for NB and dmNB in case of Pt/C, featuring surface located Pt NPs. In contrast, the UiO-66 based hybrid materials show a conversion as low as 0.2 % (Pd1Pt1@UiO-66) and 0.5 % (Pt@UiO-66). This strongly supports the complete and successful encapsulation of the metal NPs within UiO-66 as the diffusion of dmNB into the MOF is not favored due to the molecule size.

Independent testing of both substrates separately showed the potential of those catalysts for shape-selectivity. Additionally, the catalytic experiments were conducted with both substrates simultaneously (Figure 5c). The catalytic tests demonstrate the performance and simultaneous sieving behavior of the NP@UiO systems. Especially Pd1Pt1@UiO-66 (blue) with an equal molar

metal ratio show enhanced activity towards the conversion of NB, similar to the observed results from the preliminary studies (Figure 5a), while Pt@UiO-66 (red) is consequently less active. Furthermore, Pd1Pt2@UiO-66 with a thicker shell of Pt was tested. The obtained slope (orange) of the NB conversion proceeds similar to that of Pt@UiO-66 with decreased formation speed to aniline. This reveals the importance of the shell thickness and composition in general. It is known from literature that thinner shells can give higher shell metal dispersion as well as stronger core/shell interactions, thus resulting in a higher activity.[13, 29] Therefore, it is assumed that the thick Pt shell eliminates or strongly reduces the positive electronic effect of the core metal (Pd) and simultaneously prevents migration of Pd atoms to the surface as it was observed in case of Pd1Pt1 with equimolar ratio of both metals. Nevertheless, all materials are size-selective and almost no conversion of dmNB is observed within the first 3 h. In contrast, Pt/C shows no selectivity for one of the substrates. Only a slightly enhanced hydrogenation activity for NB can be found. Pd1Pt1@UiO-66 exhibits a good activity towards the NB hydrogenation with ~ 66 % conversion after 1 h of reaction, similar to Pt/C (74 %), while the reactant specific selectivity is retained (Figure 5d). This is obviously not the case for Pt@UiO-66 and Pd1Pt2@UiO-66. Both materials exhibit similar conversion with approximately 14 % for NB, which in fact confirms that the system with a thicker Pt shell can be considered as monometallic species in terms of the activity. Similar results were also obtained for the RuPt NP loaded composites (Figure S15). Both exhibit size-selective properties with enhanced selectivity for the smaller molecule NB and the tendency for decreased activity with increasing Pt shell thickness was also detected.

The observed catalytic activities for hydrogenation of both substrates under separated and simultaneous conditions were also confirmed by calculation of turnover frequencies (TOFs) derived from the kinetic data (Table 3).

It can be observed that both molecules are reduced practically at the same rate over Pt/C (TOFNB/TOFdmNB = 0.85) in separated reactions. Under reaction conditions with simultaneous use of both reactants, NB is preferentially hydrogenated compared to dmNB (TOFNB/TOFdmNB = 1.83). Nevertheless, Pt/C shows no appropriate selectivity for any of the molecules. This behavior completely changes upon the utilization of the NP@MOF based catalysts. All materials exhibit high reaction rates for NB (TOFNB/TOFdmNB > 100) without conversion of dmNB, either separated nor in the mixture. As indicated the TOFs for NB conversion of the sample with encapsulated bimetallic NPs (691 h-1) is only slightly lower than Pt/C (740 h-1). In contrast monometallic Pt in UiO-66 exhibits a much lower TOF of 121 h-1, similar to the value of Pd1Pt2@UiO-66 (119 h-1) with a thicker Pt shell. At this point it needs to be mentioned that the low conversion observed for dmNB over the MOF-based catalysts makes it difficult to provide accurate values for relative TOFs, due to the error in the calculations. Rather those values should illustrate the potential of embedded NPs with a shape-selective support material compared to surface located NPs.

Table 3. Turnover frequencies (TOFs) obtained for NB and dmNB hydrogenation separately and in an equimolar mixture of both substrates over the Pt and PdPt containing catalysts.

	TOF_{NB} [h^{-1}]		TOF_{dmNB} [h^{-1}]		TOF_{NB} / TOF_{dmNB}	
	[a]	[b]	[a]	[b]	[a]	[b]
Pt/C	880.0	740.8	1033.6	404.8	0.85	1.83
Pt@UiO-66	321.6	121.6	1.6	1.1	201	111

Pd_1Pt_1@UiO-66	790.4	691.2	1.2	0.8	659	864
Pd_1Pt_2@UiO-66	-	119.5	-	1.1		109

[a] TOFs of NB and dmNB in separated reactions. [b] Individual TOFs of NB and dmNB in an equimolar mixture of both substrates. TOFNB/TOFdmNB illustrates the NB to dmNB reaction rate ratio. The TOF values were calculated on the basis of converted substrate per mol of metal per hour at short reaction times (conversion below 30%), according to metal loadings determined by atomic absorption spectroscopy.

In fact the utilization of bimetallic NPs in UiO-66 compensates low diffusion rates through the microporous structure by an activity enhancement, with simultaneous size-selectivity. Moreover, partial substitution of Pt by cheaper metals such as Pd decrease the overall cost for rare noble metals and, therefore, the catalyst itself.

It is well established that the reaction solvent plays also a major role for the activity and selectivity of specific catalysts. For the investigation of these effects upon size-selective hydrogenation of NB and dmNB over Pt/C and Pd1Pt1@UiO-66 catalysts, different solvents, such as ethanol, ethyl acetate and toluene, were tested (Figure S16). Interestingly, the change from hexane to toluene almost doubled the reaction time needed until 100 % conversion of NB and dmNB was achieved over Pt/C. In case of the MOF based composite the decrease of the initial reaction rate with respect to hexane is much less pronounced, resulting in an inversion of the activity of both Pt/C and Pd1Pt1@UiO-66 catalysts, while Pd1Pt1@UiO-66 still maintain the size-specific substrate selectivity.

On the other hand, a change to polar solvents(ethyl acetate (EtOAc) or ethanol), reveals the formation of several side products, such as 3,5-dimethylnitrosobenzene and azoxy compounds (azoxybenzene, dimethylazoxybenzene and tetramethylazoxybenzene). It is known from literature that hydrogenation of nitro-based compounds leads to the formation of intermediates, such as nitroso and hydroxylamines, which further react to the corresponding azoxy substances.[44] Du et al. performed hydrogenation of NB using ethanol with Pt NPs supported by the mesoporous framework (MIL-101) and detected similar intermediates.[45] The conversion of the nitro-based compounds is approximately similar over Pt/C and the MOF composite in ethanol. Therefore, the MOF is competitive or even superior to Pt/C in hexane, toluene and ethanol. However, use of EtOAc as solvent significantly decreased the activity of Pd1Pt1@UiO-66 and even after 6 h the NB conversion was lower than 20 %, while Pt/C reaches 100 % after 4 h. In this case, two facts need to be considered. i) The solubility of H2 is higher in ethanol and therefore it is assumed that the reaction proceeds faster as observed with Pt/C.[46] However, this is no explanation for the significant decrease of activity in case of the MOF composite. ii) Here a strong influence of the solvent effect may be inferred. It might be that different solvation of the reactants hampers the infiltration process of NB into the pores of UiO-66, while the surface located Pt NPs at carbon are negligible affected. Albeit reactivity and selectivity are strongly depending on the solvent, the UiO-66 based samples retain their sieving properties always compared to Pt/C.

Furthermore, recycling experiments of PdPt@UiO-66 were performed. The sample showed no significant loss of reactivity and size-selectivity after three consecutive cycles (Figure S17, left). Powder XRD measurements confirm the integrity of crystalline UiO-66 after the catalytic runs

(Figure S17, right) and reflections belonging to metal NPs were not detected. Additionally, TEM of the hybrid material after catalysis (3 runs) was measured (Figure S18). The images verify the intactness of the MOF crystals with core-located PdPt NPs. The formation of PdPt NPs at the outer surface of the crystallites, caused by metal migration, is not observed. Agglomeration and growth of NPs was also excluded, as the average size of the particles after catalysis was measured to be 4.1 ± 0.7 nm and therefore similar to those of the material before catalysis (4.2 ± 0.8 nm).

Evaluation of CO oxidation over RuPt NPs

In 2008, the group of Eichhorn intensively studied RuPt NPs with core located Ru and thin Pt layers for the preferential oxidation of CO in excess hydrogen.[36] Interestingly, the utilized core/shell systems exhibit the highest catalytic performance for preferential oxidation of CO among all other utilized particles, including Ru, Pt, and alloyed particles as well as physical mixtures. The origin of the activity of RuPt core/shell particles was attributed to changes in the electronic structure of surface-located Pt species as evidenced by DFT calculations. At the light of these observed effects, we decided to test the catalytic performance of our Pt and Ru1Pt1 NPs embedded in UiO-66 for CO oxidation in presence and absence of hydrogen (Figure S19)

The accessibility of the PVP coated encapsulated NPs was confirmed by the resulting activity, as non-loaded UiO-66 (Figure S19, green line) showed no activity over the whole temperature range either in H2 or He. Conversion of CO over the NP@UiO-66 catalysts reveals a clear temperature shift towards lower temperatures for the system with the bimetallic species as compared to monometallic NPs. In excess hydrogen atmosphere the onset (light-off) of CO conversion over Ru1Pt1@UiO-66 is observed at 115 °C, while 50 % conversion is achieved at 130 °C. In case of Pt@UiO-66, conversion starts approximately at 170 °C, but only 50 % conversion is obtained until the maximum measured temperature of 200 °C. The results indicate the higher catalytic activity of the bimetallic RuPt NPs due to synergetic effects under hydrogen atmosphere with a difference of approximately 70 °C (T50) compared to monometallic Pt NPs. For comparison, further reactions were conducted under exclusion of hydrogen. Surprisingly, it was found that Ru1Pt1@UiO-66 shows even higher activity in absence of hydrogen with temperatures around 120 °C. On the contrary, the temperature of Pt@UiO-66 shifts towards higher values (~ 240 °C). In a precedent study by Zhang et al. on similar systems (Pt@UiO-66) with preformed NPs, full CO conversion was already observed at 180 °C.[22] Obviously, the used conditions (gas flow, gas concentration, heating ramp, etc.) as well as the equipment strongly influence the final activity and direct comparison to literature is rather difficult.

Nevertheless, CO conversion with this specific set-up illustrates the superior properties of the bimetallic NPs, as full conversion was reached at half of the temperature compared to monometallic Pt NPs (□T = 120 °C). In order to elucidate that the support has no crucial effect on the CO conversion, as the catalytic findings for RuPt NPs were very different from those of the published ones,[36] we reproduced the systems, with Al2O3 support, according to literature. Utilization of similar conditions as for the loaded MOFs, shows no significant difference of temperatures in case of the Al2O3 supported NPs (Table 4). This implies that the support itself has no direct or only a slight impact on the overall activity in this particular case. Ru1Pt1@Al2O3

(147 °C) exhibits slightly higher temperatures towards CO oxidation with respect to the MOF analog (130 °C), while the observed trend of lower needed temperatures in helium was similarly present (H2 = 147 °C vs. He = 127 °C). Pt@Al2O3 exhibits conversion of 50 % at T50 = 269 °C, which is 30 °C higher in comparison to Pt@UiO-66, probably caused by the larger Pt NPs size (~ 6 nm), which were prepared by reduction in ethylene glycol instead of methanol (Pt@UiO-66). Table 4 summarizes the obtained CO oxidation in H2 and He.

Table 4. Catalytic activity of the UiO-66 and Al2O3 based systems on basis of the temperature at 50 % CO conversion (T50) in hydrogen or helium, respectively. The concentration for the reactive gases was set to 0.25 % for CO and 0.5 % for O2.

Gas	Temperature (T_{50}) [°C]			
	Pt@UiO-66	Ru_1Pt_1@UiO-66	Pt@Al_2O_3	Ru_1Pt_1@Al_2O_3
Hydrogen	~ 200	130	-	147
Helium	237	118	269	127

The integrity of the materials after the catalytic reaction was confirmed by powder XRD measurements (Figure S20). No signals for agglomeration or sintering of NPs were detected, which, in fact, proofs the stabilization effect by the host matrix UiO-66.

Conclusions

In summary, the encapsulation of preformed bimetallic NPs into the thermally and chemically robust Zr-based UiO-66 and its derivatives UiO-66-NH2 and UiO-66-NO2 was demonstrated for the first time. The applied concept combines the utilization of a stable with a more labile metal in core/shell-like fashion and subsequent imbedding into Zr-based MOFs without the abandonment of the important precursor ZrCl4. Due to the formation of hydrochloric acid during the solvothermal synthesis and the harsh conditions (120 °C), the encapsulation process is strongly limited to very stable metals. Pt proved to be promising for the utilization as protective metal as it indicates successful encapsulation into UiO-66 without strong leaching behavior. We faced the problem with monometallic Pd NPs, which show strong aggregation and almost complete leaching during the solvothermal synthesis. Therefore, direct encapsulation was challenging and no appropriate NP@MOF systems with exclusively embedded NPs were obtained. However, following the protective synthetic path, enabled the successful encapsulation of PdPt core/shell NPs into UiO-66 with different metal compositions. The resulting PdPt@UiO-66 materials show excellent catalytic performance for the hydrogenation of nitrobenzenes, compared to their monometallic counterpart Pt@UiO-66, with simultaneous shape-selectivity for different sized substrates. The stability of the catalyst was proven by recycling experiments, with no significant change of the catalyst (NP size, crystallinity) or the catalytic performance. Moreover, the multi-metal induced catalytic activity and substrate specific selectivity of the microporous support could even surpass the performance of commercially available Pt/C, especially with view to selectivity. Further, the concept was transferred to other UiO-66 derivatives and also RuPt core/shell particles were successfully incorporated into the Zr-based MOF. The RuPt@UiO-66 materials show high catalytic activity for the oxidation of CO, compared to Pt@UiO-66. All together the findings demonstrate the great

potential and the beneficial properties of metal@MOF-based materials with bimetallic species for catalytic processes. Application of bimetallic particles seems to balance diffusion limitations of the porous support compared to surface located Pt NPs (Pt/C) without loss of general shape- and size-selectivity. As the situation of the particle surfaces was not completely clear, further studies will concentrate on the exact NP composition before and after hydrogenation reactions in future. The manufacture of NP@MOF composites with multi-metallic NPs remains an attractive research field, especially in view to environmental and economically relevant reasons, and will be interesting for several other applications as well.

Experimental Section

Materials: All chemicals were purchased from commercial suppliers (Sigma-Aldrich, Alfa Aesar, Acros Organics and others) and used without further purification.

Characterization Methods: Powder X-ray diffraction (PXRD) measurements were recorded in flat mode with an X'Pert PRO MRD PANalytical equipment in Bragg–Brentano geometry, with a PIXcel position sensitive detector and a CuKα radiation source (λ = 1.54178 Å) at room temperature. FTIR spectra were measured with a Bruker Alpha-P FTIR spectrometer equipped with a single-reflection diamond ATR module under inert gas conditions. Nitrogen sorption measurements were performed with a 3Flex Surface Characterization Analyzer instrument from Micromeritics with nitrogen gas (99.9995%) at 77 K. The specific surface areas were calculated using the sorption data in the relative pressure range from 0.05 to 0.2 bar. Prior to the measurements, all samples were evacuated in dynamic vacuum (p = 10–6 mbar) at 100 °C for 6 h. The elemental composition of the compounds was measured at the Mikroanalytisches Labor Kolbe in Mülheim an der Ruhr, Germany. Thermogravimetric analysis was performed with a Netzsch STA 409 PC/PG instrument (sample weight approximately 5–10 mg) in a temperature range from 303 to 1073 K with a heating ramp of 5 Kmin–1 at atmospheric pressure and under a stream of nitrogen (99.999%, 300 mLmin–1). X-ray photon spectroscopy (XPS) was performed with a Physical Electronics PHI 5000 VersaProbe spectrometer, using a standard Al Ka source (1486.6 eV) powered at 300 W. The working pressure was lower than 10-7 mbar. Reported binding energy (BE) were charge effect corrected by assigning a BE of 284.8 eV to the adventitious C1s signal. Ar+ sputtering was carried out at 3 kV and a 0.5 mA cm-2 beam current density with an argon partial pressure of 5 × 10-8 mbar. The measurements were performed at the Faculty of Physics and Astronomy, Department of Experimental Physics II, Ruhr-University Bochum. Transmission electron microscopic measurements were carried out with a Tecnai G2 F20 and a Philips CM20 with an acceleration voltage of 200 kV at the department of Mechanical Engineering, Ruhr-University Bochum, Germany. Energy-dispersive X-ray spectroscopy was performed at the Tecnai G2 F20. Annular dark field scanning transmission electron microscopy (ADF-STEM) and high resolution ADF-STEM images were recorded using an aberration corrected FEI Titan 'Cubed' 60-300 transmission electron microscope, operated at 200 kV. The inner collection semi-angle of the ADF-STEM detector was approximately 32 mrad and the probe convergence semi-angle 21 mrad. High-angle annular dark-field scanning transmission electron microscopy and energy-dispersive X-ray spectroscopy were performed at the Research Laboratory of High- Voltage Electron Microscope, Kyushu University, Japan, recorded with a JEM-ARM200F operating at 200 kV.

Synthesis of metal nanoparticles

PVP stabilized Pt NPs

The Pt NPs were synthesized by a slightly modified procedure of Lu et al.[21] Therefore, a mixture of PVP (399 mg, 3.6 mmol, Mw=55.000), methanol (540 ml) and an aqueous solution of H2PtCl6 (6 mM, 60 ml) was refluxed for 3 h under air. Afterwards methanol was removed with help of a rotary evaporator and the Pt particles in the remaining solution were precipitated with acetone. Subsequently, the particles were separated by centrifugation at 7000 g for 3 minutes and washed several times with ethanol and ether for the removal of excess free PVP. Drying of the precipitated particles under reduced pressure (10-3 mbar) results in a black powder.

PVP stabilized Pd NPs

Pd NPs were synthesized by the reduction of H2PdCl4 with ethanol. A 2 mM H2PdCl4 solution (100 mL, 0.2 mmol) was mixed with PVP (23 mg, 0.2 mmol) and H2O (560 mL). Under vigorous stirring, ethanol (160 mL) was added and the mixture was heated to reflux for 3 h. Afterward the brown solution was cooled to room temperature, and the solvent was removed by evaporation. The dark brown residue was redissolved and washed several times with ethanol. The particles were collected by centrifugation and dried under vacuum (p =10–3 mbar) for 12 h to yield a dark brown product.

PVP stabilized core/shell Pd1Pt1 and Pd1Pt2 NPs

The synthesis was done by a modified procedure of Wang et al.[30] The prepared Pd NPs (core material) were dispersed in a 150 ml mixture of water-ethanol-ethylene glycol (1:1:1) in a 500 ml flask which was equipped with a dropping funnel and a connection to hydrogen (99.999 %). The dropping funnel was charged with a degassed aqueous solution (100 ml) of K2PtCl4 (83 mg, 0.2 mmol) which was kept under Argon atmosphere. The air of the flask with the Pd colloid was replaced by a hydrogen atmosphere and the colloid was allowed to stay under these conditions for 2 h under stirring. Subsequently, the K2PdCl4 solution was added drop wise into the reaction system within 6 h and the reaction was continued for another 8 h. Afterwards the PdPt NPs were collected by centrifugation, washed several times with EtOH and dried under vacuum (p =10–3 mbar) for 12 h. To avoid any oxidation the particles were stored under an inert gas atmosphere until usage. Similarly, core/shell particles with a thicker Pt shell (named as Pd1Pt2) were synthesized. But instead of a 100 ml K2PtCl4 solution, 200 ml of a K2PtCl4 (166 mg, 0.4 mmol) solution were used.

PVP stabilized core/shell Ru1Pt1 and Ru1Pt2 NPs

The RuPt NPs were synthesized by a procedure of Alayoglu et al.[36] Ru(acac)3 (80 mg, 0.2 mmol) and PVP (55 mg, 0.5 mmol) are dissolved in 40 ml ethylene glycol. Subsequently the Ru NPs (core metal) are synthesized by a fast temperature ramp and subsequent refluxing for 3 h under stirring and Argon atmosphere. When the colloidal Ru NP solution was cooled down to room temperature, PtCl2 (54 mg, 0.2 mmol) was added and the mixture was heated slowly with 1-2 K min-1 to reflux and kept at this conditions for 1.5 h. Afterwards the Ru1Pt1 NPs were collected by centrifugation, washed several times with EtOH and dried under vacuum (p =10–3

mbar) for 12 h. To avoid any oxidation the particles were stored under an inert gas atmosphere until usage. For the synthesis of core/shell particles with a thicker layer of Pt, the amount of $PtCl_2$ added was doubled.

Synthesis of UiO-66 and NP@UiO-66

UiO-66

In a typical synthesis $ZrCl_4$ (612 mg, 2.63 mmol) was dissolved in 600 ml N,N-Dimethylformamide (DMF) in a teflon-capped 1 l glass flask. Subsequently, 36 ml of acetic acid were added and the mixture was allowed to sonicate for 20 min. Afterwards, Terepthalic acid (435 mg, 2.62 mmol) was added and the solution was treated for another 20 min in an ultrasonic bad. Solvothermal synthesis was done in an oven at 120 °C for 24 h. When the solution was cooled down to room temperature, the white precipitate was collected and washed three times with fresh DMF (30 ml). Additionally the washing procedure includes 3 periods of fresh DMF exchange after 6 h, respectively. Afterwards DMF was exchanged with MeOH (3 times, 30 ml). Finally, the material was dried in vacuum (p = 10-3 mbar) at room temperature for 24 h and stored inside a glovebox.

UiO-66(NH_2) and UiO-66(NO_2)

$ZrCl_4$ (51.3 mg, 0.220 mmol) was dissolved in 50 ml DMF in a Teflon-capped 100 ml glass flask. Afterwards, 3 ml acetic acid were added and the mixture was sonicated for 20 min. Subsequently, 2-Aminoterephthalic acid (39.9 mg, 0.220 mmol) or 2-Nitroterephthalic acid (46.4 mg, 0.220 mmol) was added and the mixture was allowed to sonicate for another 20 min. The solvothermal synthesis was done for 24 h at 120 °C. After cooling to room temperature the precipitate was collected. The washing and drying procedure is similar to normal UiO-66.

PdPt@UiO-66

The synthesis of PdPt@UiO-66 is similar to pristine UiO-66, but after the last sonication step a colloidal dispersion of the particles (30 mg dissolved in 30 ml DMF) was added. The reaction mixture was agitated for 10 sec and then allowed to react at 120 °C for 24 h without stirring, resulting in a brown-black precipitate.

RuPt@UiO-66

The synthesis of RuPt@UiO-66 was similar to PdPt@UiO-66, but instead RuPt NPs were used. The solvothermal reaction with the RuPt NPs results in a grey powder.

Catalytic hydrogenation of nitrobenzenes

The competitive hydrogenation of nitrobenzene (0.25 mmol) and 3,5-dimethylnitrobenzene (0.25 mmol) was carried out at ambient temperature inside 2 mL reactors pressurized at 2 bars H2, with 1 ml of hexane, ethanol , ethyl acetate or toluene, respectively. The catalyst amount for each run was adjusted to 0.06 mol-% metal with respect to both compounds. Liquid reaction products were analyzed by GC and GC-MS. Catalytic Reusability of the catalyst was performed in ethanol. After each cycle, the solid catalyst was recovered by filtration and washed thoroughly with ethanol. After drying in vacuum (10-3 mbar) overnight the catalyst was reused.

CO oxidation

A U-shaped quartz reactor was loaded with 20 mg catalyst diluted in 80 mg silicon carbide and placed in a continuous flow set-up. Prior to CO oxidation, a reductive pretreatment in hydrogen atmosphere at 200 °C was performed. The catalytic oxidation of CO was performed in a gas mixture of 0.25 % CO (minimal value limited by accurarcy of the mass flow controllers used) and 0.5 % O2 diluted in helium or hydrogen with a total flow rate of 100 mL min-1. Prior to CO oxidation a reductive pretreatment of the catalysts was done. First pure helium was purged for 15 min through the reactor. Afterwards, the rector was heated up to the final pretreatment temperature (200 °C) with 1 K min-1 in a flow of 100 mL min-1 in 10 % hydrogen and maintained at this temperature for 60 min, before the system was allowed to cool down to room temperature. Subsequently the reactor was purged with He and the desired reaction mixture was flushed through the reactor and the sample was heated to 200 °C (carrier gas H2) and 300 °C (carrier gas He) with a heating rate of 1 Kmin-1. The effluent gas stream after the catalytic process was analyzed with a non-dispersive IR-detector (Hartmann&Braun, Advanced Optima URAS 14) to determine the concentration of the out coming species. Concentrations of CO and CO2 during the catalytic CO oxidation were measured by a NDIR detector.

Acknowledgements

This work is supported by the Cluster of Excellence RESOLV (EXC 1069) funded by the Deutsche Forschungsgemeinschaft (DFG).

Keywords: Metal-Organic Frameworks • Nanostructures • Nanoparticles • Catalysis

[1] H. R. Moon, D.-W. Lim, M. P. Suh, Chemical Society Reviews 2013, 42, 1807-1824.

[2] J. Juan-Alcaniz, J. Gascon, F. Kapteijn, Journal of Materials Chemistry 2012.

[3] C. R. Kim, T. Uemura, S. Kitagawa, Chemical Society Reviews 2016.

[4] J. Hermannsdörfer, M. Friedrich, N. Miyajima, R. Q. Albuquerque, S. Kümmel, R. Kempe, Angewandte Chemie 2012, 124, 11640-11644.

[5] Q.-L. Zhu, J. Li, Q. Xu, Journal of the American Chemical Society 2013, 135, 10210-10213.

[6] Z. Li, R. Yu, J. Huang, Y. Shi, D. Zhang, X. Zhong, D. Wang, Y. Wu, Y. Li, Nature Communications 2015, 6.

[7] W. Lu, Z. Wei, Z.-Y. Gu, T.-F. Liu, J. Park, J. Park, J. Tian, M. Zhang, Q. Zhang, T. Gentle Iii, M. Bosch, H.-C. Zhou, Chemical Society Reviews 2014, 43, 5561-5593.

[8] N. Stock, S. Biswas, Chemical Reviews 2011.

[9] H. Furukawa, K. E. Cordova, M. O'Keeffe, O. M. Yaghi, Science 2013, 341, DOI: 10.1126/science.1230444.

[10] C.-J. Jia, F. Schuth, Physical Chemistry Chemical Physics 2011, 13, 2457-2487.

[11] D. Wang, Y. Li, Advanced Materials 2011, 23, 1044-1060.

[12] H. Kobayashi, K. Kusada, H. Kitagawa, Accounts of Chemical Research 2015, 48, 1551-1559.

[13] R. Ghosh Chaudhuri, S. Paria, Chemical Reviews 2012, 112, 2373-2433.

[14] R. Ferrando, J. Jellinek, R. L. Johnston, Chemical Reviews 2008, 108, 845-910.

[15] Y. Huang, Y. Zhang, X. Chen, D. Wu, Z. Yi, R. Cao, Chemical Communications 2014, 50, 10115-10117.

[16] J. Zhou, P. Wang, C. Wang, Y. T. Goh, Z. Fang, P. B. Messersmith, H. Duan, ACS Nano 2015.

[17] L. Chen, B. Huang, Q. Xuan, X. Wang, R. Luque, Y. Li, Chemical Science 2015.

[18] L. Chen, X. Chen, H. Liu, Y. Li, Small 2015, 11, 2642-2648.

[19] C. Rösler, D. Esken, C. Wiktor, H. Kobayashi, T. Yamamoto, S. Matsumura, H. Kitagawa, R. A. Fischer, European Journal of Inorganic Chemistry 2014, 2014, 5514-5521.

[20] Y. Liu, Z. Tang, Advanced Materials 2013, 25, 5819-5825.

[21] G. Lu, S. Li, Z. Guo, O. K. Farha, B. G. Hauser, X. Qi, Y. Wang, X. Wang, S. Han, X. Liu, J. S. DuChene, H. Zhang, Q. Zhang, X. Chen, J. Ma, S. C. J. Loo, W. D. Wei, Y. Yang, J. T. Hupp, F. Huo, Nature Chemistry 2012, 4, 310-316.

[22] W. Zhang, G. Lu, C. Cui, Y. Liu, S. Li, W. Yan, C. Xing, Y. R. Chi, Y. Yang, F. Huo, Advanced Materials 2014, 26, 4056–4060.

[23] J. H. Cavka, S. Jakobsen, U. Olsbye, N. Guillou, C. Lamberti, S. Bordiga, K. P. Lillerud, Journal of the American Chemical Society 2008, 130, 13850-13851.

[24] I. Luz, C. Rösler, K. Epp, F. X. Llabrés i Xamena, R. A. Fischer, European Journal of Inorganic Chemistry 2015, 2015, 3904-3912.

[25] M. Kandiah, M. H. Nilsen, S. Usseglio, S. Jakobsen, U. Olsbye, M. Tilset, C. Larabi, E. A. Quadrelli, F. Bonino, K. P. Lillerud, Chemistry of Materials 2010, 22, 6632-6640.

[26] Z. Hu, D. Zhao, Dalton transactions 2015, 44, 19018-19040.

[27] K. Tulig, K. S. Walton, RSC Advances 2014, 4, 51080-51083.

[28] I. Saldan, Y. Semenyuk, I. Marchuk, O. Reshetnyak, Journal of Materials Science 2015, 50, 2337-2354.

[29] P. Zhang, Y. Hu, B. Li, Q. Zhang, C. Zhou, H. Yu, X. Zhang, L. Chen, B. Eichhorn, S. Zhou, ACS Catalysis 2015, 5, 1335-1343.

[30] Y. Wang, N. Toshima, The Journal of Physical Chemistry B 1997, 101, 5301-5306.

[31] T. Rades, V. Y. Borovkov, V. B. Kazansky, M. Polisset-Thfoin, J. Fraissard, The Journal of Physical Chemistry 1996, 100, 16238-16241.

[32] G. M. Bancroft, I. Adams, L. L. Coatsworth, C. D. Bennewitz, J. D. Brown, W. D. Westwood, Analytical Chemistry 1975, 47, 586-588.

[33] H. Liu, L. Chang, L. Chen, Y. Li, J. Mater. Chem. A 2015, 3, 8028-8033.

[34] J. F. Moulder, W. F. Stickle, P. E. Sobol, K. D. Bomben, Handbook of X-ray Photoelectron Spectroscopy, Perkin Elmer Corporation, Eden Prairie, Minnesota, USA, 1992.

[35] Y. K. Du, P. Yang, Z. G. Mou, N. P. Hua, L. Jiang, Journal of Applied Polymer Science 2006, 99, 23-26.

[36] S. Alayoglu, A. U. Nilekar, M. Mavrikakis, B. Eichhorn, Nature Materials 2008, 7, 333-338.

[37] F. A. Westerhaus, R. V. Jagadeesh, G. Wienhöfer, M.-M. Pohl, J. Radnik, A.-E. Surkus, J. Rabeah, K. Junge, H. Junge, M. Nielsen, A. Brückner, M. Beller, Nature Chemistry 2013, 5, 537-543.

[38] R. Adams, F. L. Cohen, Organic Syntheses 1928, 8, 66.

[39] P. M. G. Bavin, Organic Syntheses 1960, 40, 5.

[40] C. F. H. Allen, J. VanAllan, Organic Syntheses 1942, 22, 9.

[41] A. Corma, P. Serna, Science 2006, 313, 332-334.

[42] A. Corma, C. Gonzalez-Arellano, M. Iglesias, F. Sanchez, Applied Catalysis A. General 2009, 356, 99-102.

[43] L. Chen, H. Chen, R. Luque, Y. Li, Chemical Science 2014, 5, 3708-3714.

[44] L. Cisneros, P. Serna, A. Corma, Angewandte Chemie International Edition 2014, 53, 9306-9310.

[45] W. Du, G. Chen, R. Nie, Y. Li, Z. Hou, Catalysis Communications 2013, 41, 56-59.

[46] M. S. Wainwright, T. Ahn, D. L. Trimm, N. W. Cant, Journal of Chemical & Engineering Data 1987, 32, 22-24.